

Spatially resolving classical and quantum entanglement with structured photons

Cade Peters , Pedro Ornelas , Isaac Nape , and Andrew Forbes 
School of Physics, University of the Witwatersrand, Private Bag 3, Wits 2050, South Africa

 (Received 26 July 2023; accepted 5 October 2023; published 3 November 2023)

Nonseparability in classical and quantum states of light gives rise to the notions of classical (local) and quantum (nonlocal) entanglement, usually defined as global features of the fields and states. Here we use concurrence as a measure of this nonseparability and show that it can be spatially resolved, revealing regions of maximum nonseparability and regions with no nonseparability. We use the topical examples of vectorial structured light and its quantum analog, a hybrid spatial mode and polarization entangled states, to test the approach on both local and nonlocal forms of entanglement. Our work has wide reaching implications, for instance, in understanding the spatial dependence of coherence and polarization in vectorial light, as well as in quantum entangled states for imaging, where spatial correlations are vital.

DOI: [10.1103/PhysRevA.108.053502](https://doi.org/10.1103/PhysRevA.108.053502)

I. INTRODUCTION

Classical and quantum states of structured light have gained in prominence of late [1,2], driven by a versatile toolbox and a myriad of exciting applications. Such states can be structured in 1 degree of freedom (DoF), for instance, the photonic orbital angular momentum (OAM) [3], or in a hybrid state of 2 or more DoF [4]. Particularly interesting examples are hybrid entangled states that mix polarization and spatial modes (such as OAM states) [5] shown in Fig. 1(a) and their classical counterpart, vectorial structured light [6], shown in Fig. 1(b), nonseparable states of light with inhomogeneous polarization structures [7]. The former are a nonlocal form of entanglement with the correlations across two or more photons that may be distantly apart, while the latter are a local form of entanglement in single-photon states and are a measure of nonseparability in classical fields. The latter are sometimes called classically entangled [8,9], but here limited to the local nonseparability of 2 or more DoF, where a measurement on one affects the outcome of the other. The local form of this nonseparability has given rise to exotically structured light, from the well-known cylindrical vector vortex beams of optical fiber [10] to light with topology, from Möbius strips [11] to skyrmions [12], fueling many applications [6], revealing the interplay between classical and quantum systems [13–15] as well as being a probe into the fundamental nature of polarization, coherence, distinguishability, and entanglement [16,17].

In parallel, quantum entanglement in the spatial basis has exploded in popularity of late, driven by interest in OAM entanglement [18,19], marking two decades since its first inception [20]. Entanglement in higher dimensions has garnered significant interest in the fields of quantum communications [21] and computation [22], leading to the development of several methods to increase security [23], computational

power [24], and resilience to noise [25]. Entanglement in the continuous position basis, in particular, has given rise to several techniques for quantum imaging [26] and quantum key distribution [27]. In these applications and others, the number of correlations and the spatial distribution of these correlations are of particular importance. Significant effort has gone into measuring the Einstein-Podolsky-Rosen-like spatial correlations between photons produced through spontaneous parametric down-conversion (SPDC) [28–33], thus allowing for the quantification and certification of spatial entanglement. It has also been shown that these spatial correlations can be manipulated and shaped, primarily for pre- and postcorrection through scattering media, by manipulating the second-order quantum coherence of the two-photon state [34,35]. Increased efficiency in measuring and certifying entanglement has also been demonstrated by spatially tailoring the basis for minimal losses, noise resistance, and fewer necessary measurements [36]. Different techniques and methods for tailoring and shaping spatial correlations and thus the nonseparability of quantum states hold tremendous potential for increasing the effectiveness of established and emerging quantum techniques.

Despite the advances, spatial entanglement (classical and quantum) is usually measured as a global property of the field or state, tracing out the spatial information. Here we use a spatially resolved projective measurement of local and nonlocal entanglement to show that the nonseparability can vary dramatically across the state, from regions of maximal nonseparability to regions of no nonseparability, shown in Fig. 1(c). Classically, the homogeneity of the fields likewise changes from fully vector to fully scalar across the field, while in quantum the correlations rise and fall in spatial regions. We use hybrid combinations of OAM beams to demonstrate the effect experimentally with a range of hybrid states and regions of interest, showing good agreement with theory. The results show that classical and quantum light can be tailored spatially for on-demand nonseparability, where some regions can differ substantially from the average (global) value. Our results offer

Corresponding author: andrew.forbes@wits.ac.za

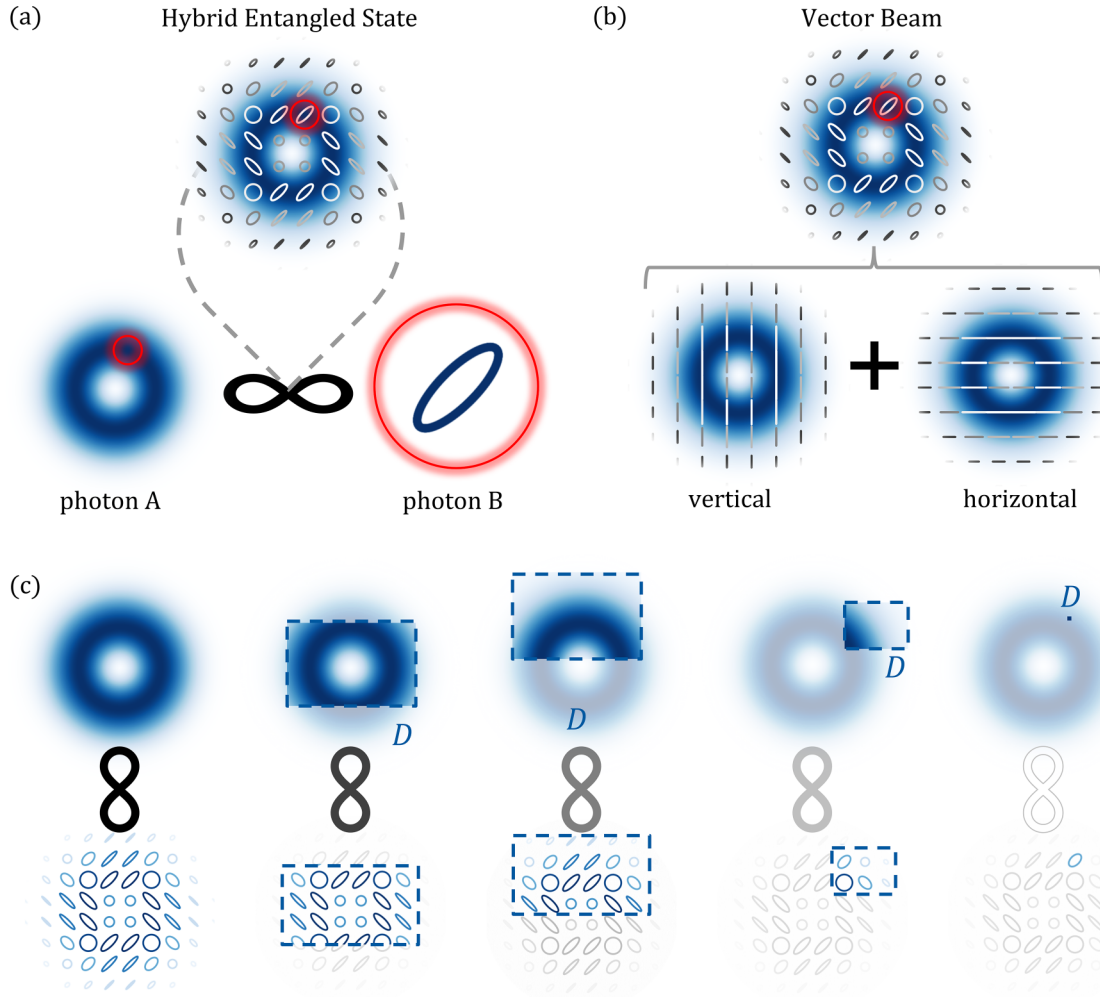


FIG. 1. Quantum and classical nonseparability. (a) Quantum hybrid entangled states correlate the spatial information of one photon (photon A) with the polarization of another (photon B) and, consequently, these two pieces of information cannot be known separately. If a position measurement is made on photon A, one will immediately know the polarization of photon B. This does not depend on the distance between the two photons and thus we have nonlocal nonseparability. (b) In a vector beam, the polarization varies spatially resulting in correlations between the spatial and polarization degrees of freedom of the beam. Every point in the beam is associated with a specific polarization state and thus one cannot speak about a position on the beam without also knowing the polarization at that position. This is a form of local nonseparability. (c) Spatial regions of the nonseparable state, which vary in size, location, and shape, exhibit different degrees of nonseparability. This suggests that the size, shape, and location of the region an observer is interested in will affect the strength of the correlations observed. A point in space has only one polarization state associated with it and therefore has no nonseparability.

insights into the spatial nature of the correlations, classical and quantum, and have wide reaching implications, for instance, in understanding the spatial dependence of coherence and polarization in vectorial light, as well as in quantum entangled states for imaging, where spatial correlations are vital.

II. THEORY

A. Quantifying nonseparability

The unique property of nonseparability, which mathematically distinguishes quantum *nonlocal* correlations from those that are classical or separable in nature, can also be used analogously to describe light beams with inhomogeneous polarization states [37,38]. In the former, the system's nonseparability is shared between two spatially separated particles, whereas in the latter the nonseparability exists *locally* between

the internal degrees of freedom of each photon in a coherent light beam. In the case where the wave functions that describe the system are position dependent, it is imperative to ask whether the domain over which the state is sampled, the resolution, and the geometry have an impact on the degree of the entanglement that can be measured.

To elucidate and answer these questions, we employ hybrid (nonlocal) entangled two photon states as well their classical analogs, i.e., light fields with inhomogeneous polarisations, also called vector beams. Both states can be expressed using the bra-ket notation following the Schmidt decomposition,

$$|\Psi\rangle = |\psi_1\rangle_A |P^+\rangle_B + |\psi_2\rangle_A |P^-\rangle_B, \quad (1)$$

where $|\psi_{1(2)}\rangle$ are arbitrary and orthogonal spatial modes, and P^\pm are orthogonal polarization eigenstates. Here our states constitute independent degrees of freedom which can be seen

from the tensor product structure, $|\text{spatial}\rangle \otimes |\text{polarization}\rangle$, enabling us to distinguish the spatial and polarization components. While at first glance, the states above bare a resemblance for both hybrid entangled states and classical vectorial beams, the discrepancies can be seen when one assigns adequate labels for the subscripts A and B : in (i) hybrid entangled states, A and B represent two different photons with each photon being entangled in an independent degree of freedom (in our case we entangled the spatial degree of freedom of photon A with the polarization degree of freedom of photon B), while for (ii) vectorial beams, they label the internal degrees of freedom of a field (A is the spatial DoF and B is the polarization DoF and both of these DoFs cannot be described separately from each other).

To examine the spatial characteristics of these states, we study their spatial variations. It is useful to rewrite the state in the position basis, $|\vec{r}\rangle$ satisfying $\langle \vec{r} | \vec{r}' \rangle = \delta(\vec{r} - \vec{r}')$. It follows that the spatial modes can be expressed as $|\psi_i\rangle = \iint_{-\infty}^{\infty} \psi_i(\vec{r}) |\vec{r}\rangle d^2\vec{r}$, where $i \in \{1, 2\}$ and $\psi_i(\vec{r})$ are the position-dependent wave functions describing the spatial components. Accordingly, by substituting this into Eq. (8), we may describe the hybrid states as

$$|\Psi\rangle = \iint_{-\infty}^{\infty} |\vec{r}_A\rangle [\psi_1(\vec{r}_A) |P^+\rangle_B + \psi_2(\vec{r}_A) |P^-\rangle_B] d^2r_A. \quad (2)$$

The nonseparability of these states is quantified using a metric known as the concurrence, which, for the above state, is given by

$$C = 2\sqrt{|\langle \psi_1 | \psi_1 \rangle \langle \psi_2 | \psi_2 \rangle - |\langle \psi_1 | \psi_2 \rangle|^2}. \quad (3)$$

where the inner product $\langle \cdot | \cdot \rangle$ is defined as

$$\langle \psi_i | \psi_j \rangle = \iint_{-\infty}^{\infty} \psi_i^*(\vec{r}_A) \psi_j(\vec{r}_A) d^2r_A \quad (4)$$

When we have $C = 0$, the state is called a completely separable state; a value between 0 and 1 indicates a partially separable state and a value of $C = 1$ indicates a maximally nonseparable state. Equation (3) shows that the nonseparability depends solely on the spatial modes of our state. We therefore conjecture that by looking at specific regions of the spatial modes, we will observe values of the nonseparability that differ from the global value. An arbitrary region of interest, D , can be isolated by using an appropriate aperture function, defined as

$$f(\vec{r}_A) = \begin{cases} 1 & \text{if } \vec{r}_A \text{ is in } D, \\ 0 & \text{otherwise.} \end{cases} \quad (5)$$

This has the overall effect of bounding the function in the region D , thus simplifying the integral in Eq. (2) to

$$|\Psi\rangle = \frac{1}{N} \iint_D |\vec{r}_A\rangle [\psi_1(\vec{r}_A) |P^+\rangle_B + \psi_2(\vec{r}_A) |P^-\rangle_B] d^2r_A, \quad (6)$$

where N is a normalization factor. Physically, this corresponds to the truncation of the spatial profile of component A , which in practice can occur due to restrictions in the apertures of the optical system. The inner products defined in Eq. (4) then also simply to

$$\langle \psi_i | \psi_j \rangle = \iint_D \psi_i^*(\vec{r}_A) \psi_j(\vec{r}_A) d^2r_A \quad (7)$$

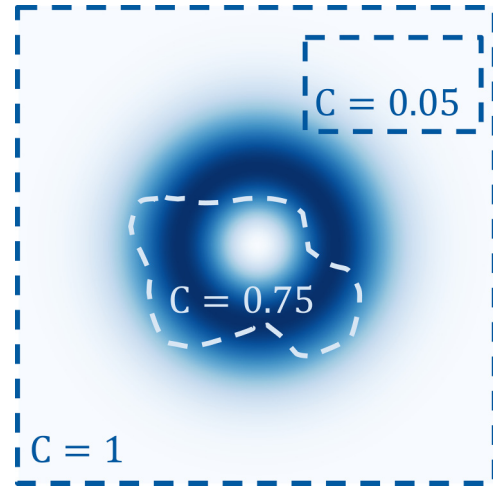


FIG. 2. The spatial dependence of nonseparability. If an observer chooses to focus on only a specific region of a vectorial light field, they will measure a different value of the field's nonseparability. This is influenced by both the location and the shape of the region of interest.

for the isolated region. In general, Eqs. (4) and (7) will not be equal and thus the nonseparability in the chosen region D will differ from the global value. This is illustrated in Fig. 2. Classically, this figure can be interpreted as showing the intensity profile of the vectorial beam. The concurrence of the different regions (shown in dashed lines) then shows the nonseparability of the different parts of the beam in the transverse plane. In the case of quantum hybrid entangled states, this figure shows the spatially resolved position probability distribution of photon A . Within each of the dashed regions, we see what the measured concurrence of the quantum state would be if we restricted the aperture of our detector to only those dashed regions. In either case, the concurrence of the entire state is 1, but if we look at specific spatial regions within the state with different locations and geometries, we measure a different value for the concurrence. Consequently, we can use the concurrence as a metric to quantify the degree of nonseparability in our chosen region of interest and allow for comparison between different regions and geometries across the state.

B. Measuring nonseparability

Concurrence can quantify the degree of nonseparability; however, Eq. (3) requires both the amplitude and the phase information for both spatial modes, which can be cumbersome to measure experimentally. Here we show that the concurrence can be measured using the spatially resolved Stokes parameters. Without loss of generality, we construct a nonseparable state in the horizontal (H) and vertical (V) polarization basis

$$|\Psi\rangle = |\psi_1\rangle_A |H\rangle_B + |\psi_2\rangle_A |V\rangle_B, \quad (8)$$

where $|\psi_{1(2)}\rangle$ are the same as above. The horizontal and vertically polarized intensity components of the state are given by

$$I_{H(V)}(\vec{r}_A) = \langle \psi_{1(2)} | \psi_{1(2)} \rangle. \quad (9)$$

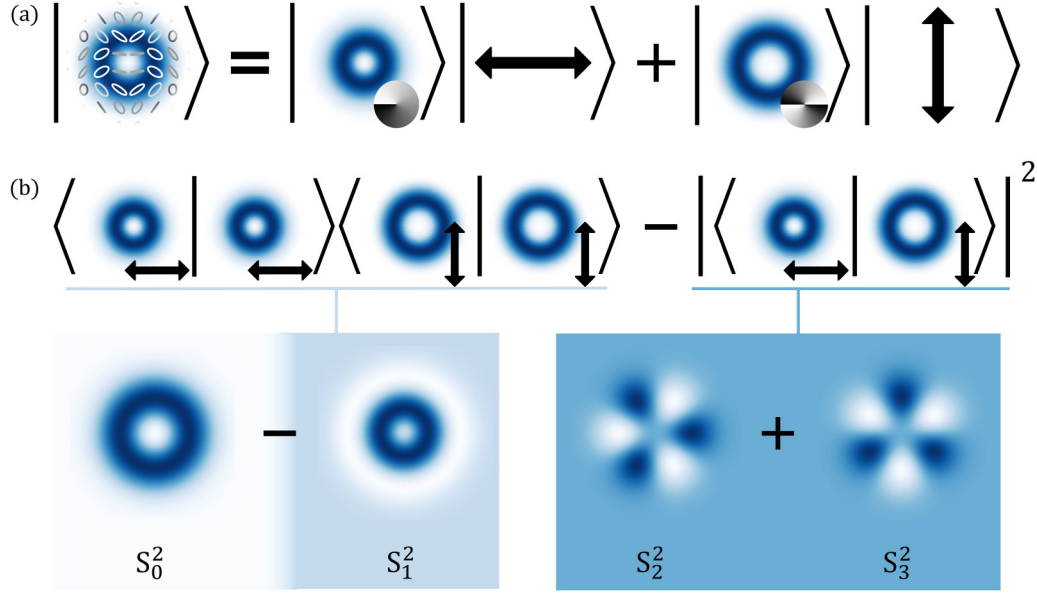


FIG. 3. Basis-independent measure of nonseparability. (a) Vector modes are created by superimposing to orthogonal scalar modes, each in an orthogonal polarization state. (b) The concurrence or nonseparability of a nonseparable state can be measured using a basis-independent method. For our states, the inner products present in the first term of Eq. (3) are directly related to the Stokes parameters S_0 and S_1 and the inner product in the second term is directly related to the Stokes parameters S_2 and S_3 . Thus the concurrence can be directly calculated from the four Stokes parameters.

The spatially varying Stokes parameters for the entire state may then be written as

$$\begin{aligned}
 S_0(\vec{r}) &= I_h(\vec{r}) + I_v(\vec{r}) = I(\vec{r}) \\
 &= I|\psi_1(\vec{r})|^2 + I|\psi_2(\vec{r})|^2, \\
 S_1(\vec{r}) &= I_h(\vec{r}) - I_v(\vec{r}) \\
 &= I|\psi_1(\vec{r})|^2 - I|\psi_2(\vec{r})|^2, \\
 S_2(\vec{r}) &= I_d(\vec{r}) - I_a(\vec{r}) \\
 &= 2I|\psi_1(\vec{r})||\psi_2(\vec{r})|\cos[\phi_1(\vec{r}) - \phi_2(\vec{r})], \\
 S_3(\vec{r}) &= I_r(\vec{r}) - I_l(\vec{r}) \\
 &= 2I|\psi_1(\vec{r})||\psi_2(\vec{r})|\sin[\phi_1(\vec{r}) - \phi_2(\vec{r})]. \quad (10)
 \end{aligned}$$

In the case of the hybrid entangled states, it is equivalent to measuring the observables of the Pauli matrices on photon B, using

$$S_j(\vec{r}) = \langle \vec{r}_A | \langle \vec{r}_A \otimes \sigma_{B,j} \rangle, \quad (11)$$

where $j \in \{0, 1, 2, 3\}$ and $\sigma_{B,0} = \mathbb{1}_2$. Full details of the calculation are given in Ref. [39]. We can obtain parameters we call the Stokes powers by integrating over the spatially resolved Stokes parameters in Eq. (10) in the chosen region D ,

$$P_i = \int_D S_i(\vec{r}) dA, \quad (12)$$

where $i \in \{0, 1, 2, 3\}$. Using the expressions in Eq. (10), we can relate the Stokes powers P_i to the inner products in Eq. (3). As shown in Fig. 3(b), the first term in the square root of Eq. (3) contains only inner products of the spatial modes with themselves and thus can give us information about the total intensity and the Stokes power directly related with our chosen basis. These are the Stokes powers P_0 and P_1 and the

exact relationship is given by

$$\begin{aligned}
 \langle \psi_1 | \psi_1 \rangle \langle \psi_2 | \psi_2 \rangle &= \int_D |\psi_1(\vec{r})|^2 dA \int_D |\psi_2(\vec{r})|^2 dA \\
 &= \frac{I_h I_v}{I^2} \\
 &= \frac{1}{4} \left[1 - \frac{P_1^2}{P_0^2} \right]. \quad (13)
 \end{aligned}$$

The Stokes powers P_2 and P_3 give the same information as the second term under the square root of Eq. (3),

$$\begin{aligned}
 \langle \psi_1 | \psi_2 \rangle &= \int_D |\psi_1(\vec{r})||\psi_2(\vec{r})| \exp\{i[\phi_1(\vec{r}) - \phi_2(\vec{r})]\} d\vec{r} \\
 &= \frac{1}{2I} \int_D S_2(\vec{r}) + iS_3(\vec{r}) d\vec{r} \\
 &= \frac{1}{2P_0} [P_2 + iP_3]. \quad (14)
 \end{aligned}$$

These relationships then allow us to rewrite the concurrence in Eq. (3) in terms of only the four Stokes powers,

$$C(D) = \sqrt{1 - \frac{P_1^2 - P_2^2 - P_3^2}{P_0^2}}. \quad (15)$$

Since we are using the concurrence as a way to quantify the nonseparability in our region of interest D , the value of C will change depending on our choice of D . This derivation shows the results for a state created in the horizontal and the vertical polarization basis. A similar argument holds for any state created in any arbitrary, orthogonal polarization basis. Using Eq. (15), we are able to easily measure and calculate the

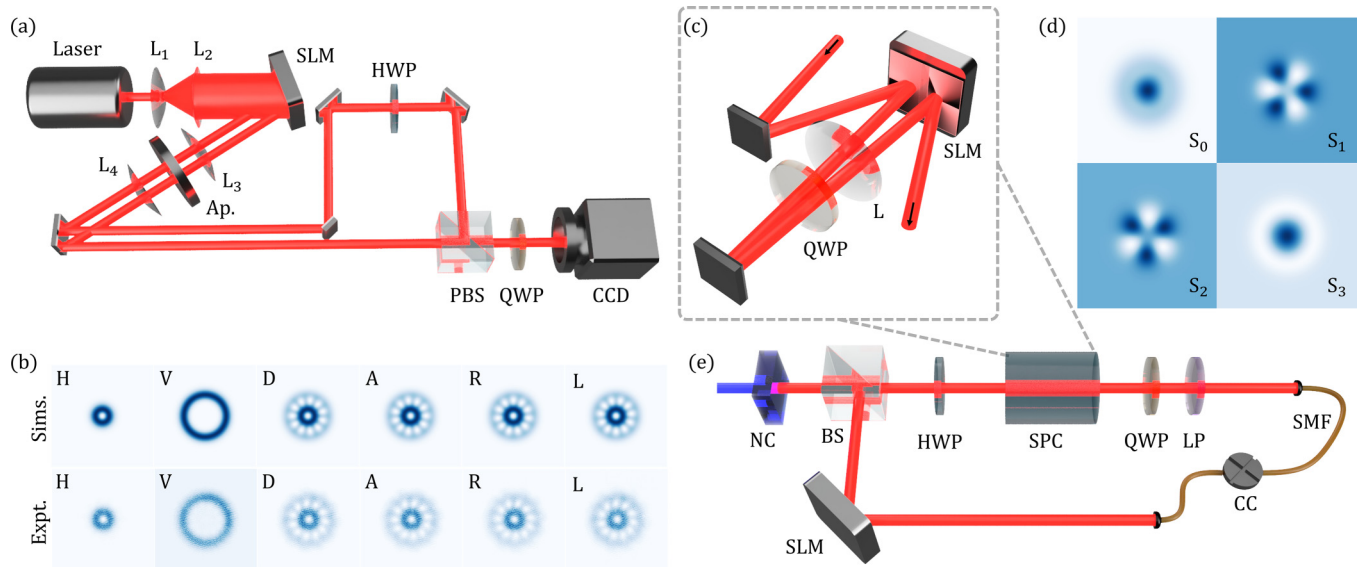


FIG. 4. Experimental setup. (a) Vector modes were generated by encoding two orthogonal spatial modes onto an SLM then combining them using a Mach-Zehnder interferometer. The beam is then directed onto a polarizer camera to obtain the four linear polarization intensities. The circular polarization intensities were obtained by placing a QWP before the camera. (b) The simulated (Sims.) and captured (Expt.) images of each polarization projection of a vector beam with $l_h = -1$ and $l_v = 10$. (c) The spatial to polarization converter (SPC) involves impinging a diagonally polarized photon onto one half of an SLM, where its horizontally polarized component is modulated. The photon then passes through a lens and QWP twice before being reflected off the second half of the SLM where the remaining light is modulated. This creates a correlation between the photon's input OAM and its output polarization. (d) The reconstructed quantum Stokes parameters of a measured hybrid entangled state with $l_1 = 0$ and $l_2 = +3$. (e) Two entangled photons are generated using a nonlinear crystal. One of the photons is incident on an SLM to determine its spatial profile. The other photon passes through a SPC to correlate its OAM to a polarization state. Its polarization is detected using polarization optics.

nonseparability of a given spatial region in an experimental setting.

III. EXPERIMENT AND RESULTS

Figure 4(a) shows the setup used to experimentally probe the spatially varying nonseparability of a vectorial beam. A green diode laser beam (wavelength $\lambda = 520$ nm) was expanded using a $10\times$ objective lens L_1 and then collimated by L_2 ($f_2 = 150$ mm) before being directed onto a reflective PLUTO-VIS HoloEye spatial light modulator (SLM). The screen of this SLM was divided into two halves. Each half was encoded with the desired scalar mode (e.g., two Laguerre-Gaussian beams, one on each half). This results in two beams in each diffraction order reflecting off the SLM. To select the desired first diffraction order, a $4f$ spatial filtering system was used. The SLM only modulates horizontally polarized light. In order to generate a vector beam, one must overlap two orthogonally polarized modes. This was achieved with a Mach-Zehnder interferometer. One beam was diverted using a system of mirrors and passed through a half-wave plate (HWP) with the fast axis at an angle of 45° , converting it from horizontally to vertically polarized. The two beams were then recombined using a polarizing beam splitter (PBS) to form a vector beam. The generated vector beam was then incident directly onto a Mako G-508 polarization-sensitive camera, which is capable of measuring all four linear polarization intensities simultaneously. The circularly polarized components were measured by placing a quarter-wave plate (QWP)

with its fast axis at an angle of 45° before the camera. This converted the right-circularly and left-circularly polarized components to horizontally and vertically polarized, respectively, which were then measured by the camera. Figure 4(b) shows the simulated (Sims.) and the experimentally captured (Expt.) polarization projections of a vector beam generated by superimposing two Laguerre-Gaussian (LG) modes. The vertically polarized mode has an OAM of 10 and the horizontally polarized mode had an OAM of -1 . Various LG modes with varying OAM were encoded to generate several different vectorial superpositions. The nonseparability for different regions of the beams was calculated using Eq. (15). The regions of interest were isolated through the use of numerical masks applied over the captured intensity images.

The setup shown in Fig. 4(e) was used to generate a hybrid entangled state. A pump beam with a wavelength of 355 nm is incident on a nonlinear crystal (NC). OAM-OAM entangled photon pairs with a wavelength of 710 nm are generated at the NC through SPDC. The photons are spatially separated using a 50:50 beam splitter (BS). One of the entangled photons, photon A, remains unchanged and is detected using the conjugate spatial OAM state on the SLM and a single-mode fiber (SMF). The other photon undergoes spatial to polarization coupling (SPC) before detection by a set of polarization optics and a SMF. Figure 4(c) shows the details of the SPC. Photon B's polarization is rotated to diagonal polarization via the use of a HWP. Photon B then impinges on one half of an SLM where the horizontal component of the polarization is modulated. The photon then reflects the SLM, through a $4f$ imaging lens

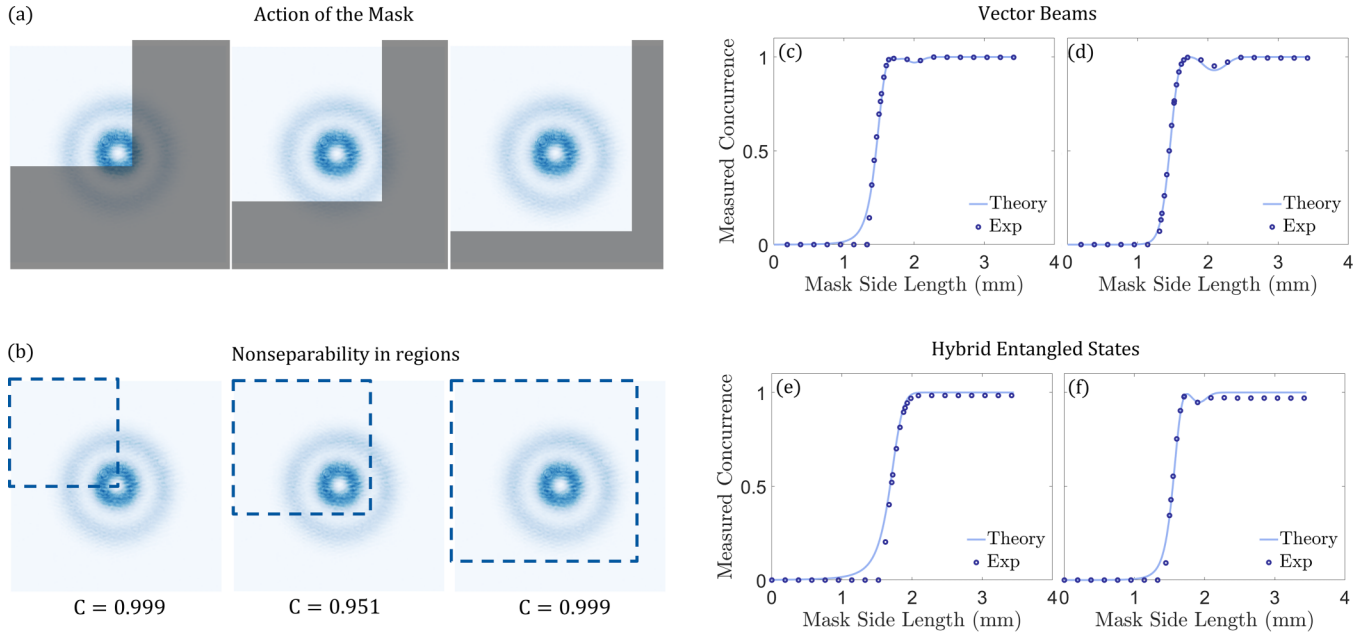


FIG. 5. Spatially varying nonseparability. (a) A square mask of increasing size was applied to the captured intensity projections allowing specific regions of the beam to be isolated and used to calculate the concurrence. (b) The nonseparability of a region is not simply a monotonically increasing function of region size but instead depends on the global geometry of the field. As the region of interest is made larger, we see that the nonseparability reaches a maximum, drops, and then returns to that maximum. Therefore, the spatially varying behavior of the nonseparability cannot be treated as simply additive. (c) The concurrence of a vector LG superposition with $l_h = -1$ and $l_v = 4$ and (d) $l_h = -1$ and $l_v = 10$ as functions of the mask size. (e) The concurrence of a hybrid entangled state with $l_1 = 0$ and $l_2 = +1$ and (f) $l_1 = 0$ and $l_2 = +3$ as functions of the mask size.

(L) and a QWP with its fast axis at 45° . This converts the horizontal and vertical polarization components to right and left circular, respectively. The photon then reflects off a mirror which flips the polarization of the right- and left-circularly polarized components. This photon then passes back through the QWP converting the circular components to horizontal and vertical. The photon then impinges on the second half of the SLM which modulates the newly horizontally polarized component (which has not been modulated by the SLM up to this point). By controlling the holograms displayed on each half of the SLM, the desired subspace can be digitally postselected. A full description of the SPC process is given in Ref. [40]. The spatially resolved quantum Stokes parameters are shown in Fig. 4(d) for a state with OAM $l_1 = 0$ and $l_2 = +3$. The regions of interest were isolated through the use of numerical masks applied over the calculated quantum Stokes parameters.

In order to first confirm that the nonseparability of the vector beam does vary spatially, a square mask of increasing size was applied to captured intensities. This procedure is shown in Fig. 5(a). The initial side length of the mask was $3.45 \mu\text{m}$ and was increased one pixel at a time to 3.45 mm . The camera's pixel size was $3.45 \mu\text{m}$. The concurrence was calculated after the application of each successive mask using Eq. (15). The results from this procedure for two different vector superpositions of LG beams are shown in Figs. 5(c) ($l_h = -1$, $l_v = 4$) and 5(d) ($l_h = -1$, $l_v = 0$). The results for this procedure applied to two different hybrid entangled states are shown in Figs. 5(e) ($l_1 = 0$, $l_2 = +1$) and 5(f) ($l_1 = 0$, $l_2 = +3$). In all cases, the component spatial modes were equally weighted resulting in a global concurrence of $C = 1$.

Simulated results are shown in light blue while experimental results are shown in dark blue. From these plots, one can see that the concurrence increases as more and more of the states are included in the region of interest until a maximum is reached. The nonseparability then has a small dip in for the two vector beams and second hybrid entangled state cases before returning to and then maintaining the maximum value. This general trend holds for all nonseparable states tested, with the dip becoming more pronounced as the difference between the OAM of the component spatial modes increases. Figure 5(b) illustrates the reason for this dip. The first maximum is reached in the first image, where exactly one quarter of the total field is included in our region of interest. The contributions from each orthogonal mode in this region are equal and thus the nonseparability is at a maximum of ≈ 1 . As the region of interest increases, as shown in the second image, the entirety of the smaller annular ring is included, while only part of the larger ring remains in the region of interest. This results in an unequal contribution from each mode and thus a drop in the nonseparability. A maximum is again reached when both modes are again included in the region of interest due to the reestablishment of equal contributions. This example is important as it illustrates that the nonseparability is not a monotonically increasing function of the size of the region of interest but also depends on the geometry of and the position relative to the global field being observed.

The primary visual feature of most states with OAM is their doughnut-shaped intensity profiles. The greater the OAM carried by the beam per photon, the larger the doughnut ring.

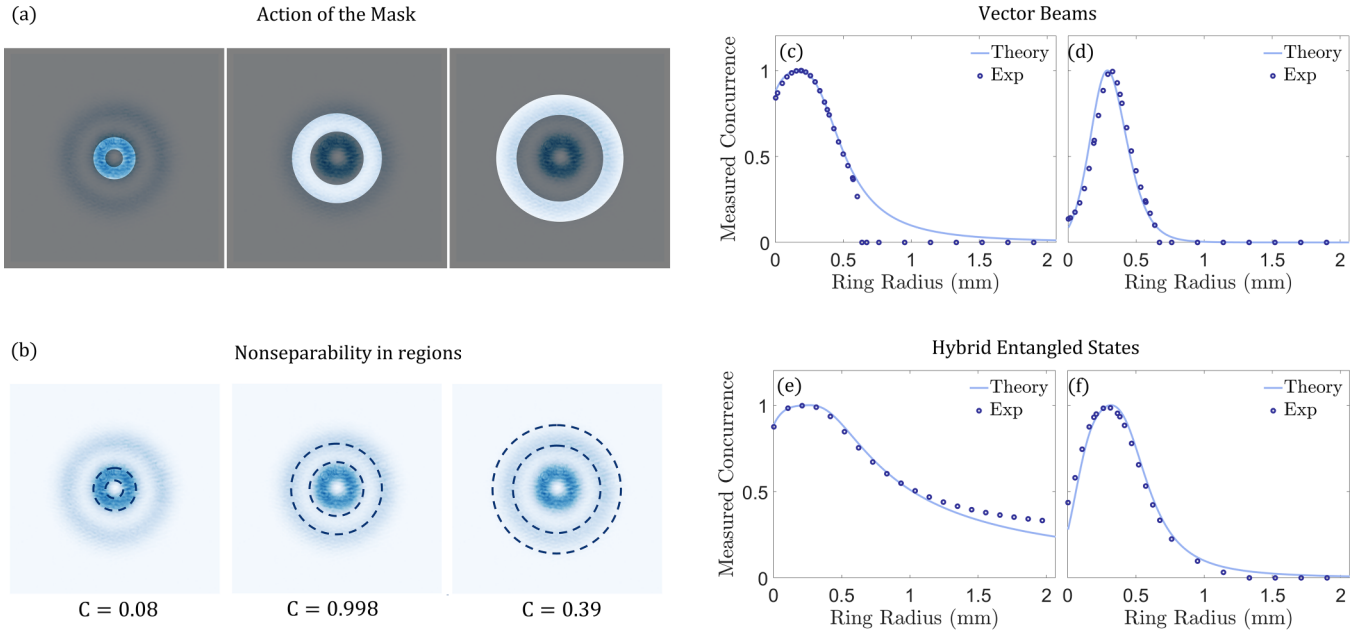


FIG. 6. Radially varying nonseparability. (a) An annular ring mask of increasing radius and fixed width was applied to the captured intensity projections, allowing specific regions of the beam to be isolated and used to calculate the concurrence. (b) Here a vector beam consisting of two LG beams with $l_h = -1$ and $l_v = 15$ is shown. The region with the intensity ring corresponding to $l_h = -1$ shows a concurrence of only $C = 0.08$, while the region corresponding to $l_v = 10$ shows a concurrence of only $C = 0.39$. The region showing the maximum concurrence is, in fact, the space between the two intensity rings. Here, the total intensity is very low compared to the rest of the state, but the relative intensities between the two spatial modes are approximately equal. This results in a very high concurrence and nonseparability even though we have a very low intensity. (c) The concurrence of a vector LG superposition with $l_h = -1$ and $l_v = 4$ and (d) $l_h = -1$ and $l_v = 10$ as functions of the annular ring's radius. (e) The concurrence of a hybrid entangled state with $l_1 = 0$ and $l_2 = +1$ and (f) $l_1 = 0$ and $l_2 = +3$ as functions of the annular ring's radius.

This creates a relationship between the OAM of the state and the spatial distribution of the beam's intensity or the spatial correlations between the entangled photons, linking the OAM subspace and the spatial distribution of the state. It is, therefore, of interest to examine how the concurrence changes as one moves through the spatial location of these OAM subspaces. To do this, a mask with an annular ring of set width (approximately 60 pixels with a pixel size of $3.45 \mu\text{m}$) was applied onto the measured intensity projections of the vector beams and the calculated quantum Stokes parameters of the hybrid entangled state. The radius of this ring was then increased until the annular ring moved past the largest intensity ring present in the vector intensity projections or quantum Stokes parameters. Each time, the concurrence was calculated according to Eq. (15). This process is illustrated in Fig. 6(a) The results of this measurement are shown for vector beams in Figs. 6(c) ($l_h = -1$, $l_v = 4$) and 6(d) ($l_h = -1$, $l_v = 10$). The vector beams were again LG superpositions. The results for two different hybrid entangled states are shown in Figs. 6(e) ($l_1 = 0$, $l_2 = +1$) and 6(f) ($l_1 = 0$, $l_2 = +3$). The results for all cases have a global concurrence of $C = 1$. The simulated results are shown in light blue and the experimental results are shown in dark blue. The plots show the nonseparability increasing until a maximum value of 1 is reached before dropping down to 0. The location of this peak shifts further outward as the difference in OAM between the two component spatial modes increases while the width of the peak decreases.

It is curious to note that the peaks observed in Figs. 6(c)–6(f) occur not when the mask is centered on any single ring, but when it is centered in between the two intensity rings. This is shown more explicitly in Fig. 6(b) for a vector beam with $l_h = -1$ and $l_v = 10$. When the annular ring mask is centered on the smaller or larger intensity rings, the concurrence is relatively low. However, when it is centered between the two intensity rings, the concurrence almost reaches the maximum possible value, suggesting that this is where most of the state's polarization inhomogeneity lies (in the case of vector beams) or where the spatial-polarization correlations are rapidly varying in position (in the case of the hybrid entangled states). This results from the fact that the spatial modes are what dictate the degree of nonseparability. At each intensity ring, contributions from a single spatial mode dominate and thus the nonseparability is quite low. In the region between the two rings, the contribution from each spatial mode are approximately equal and thus we have a high concurrence and nonseparability. We can then see that the intensity of our field does directly dictate the nonseparability and it is instead determined by the relative intensities between the the spatial modes.

IV. CONCLUSION

The ability to structure nonseparable states of light, both classical and quantum, is well known and provides a useful tool for encoding and retrieving information. Quantum structured light especially has found applications in a myriad

of fields including imaging, metrology, communications, and computing. Here we have demonstrated that the nonseparability of vectorial and quantum states is not just a property of the global state, but varies spatially, depending on the shape and location of the region of interest. Consequently and depending on the needs and context, one may alter their state to increase or decrease the nonseparability in a chosen region and quantify this change using our modified definition of concurrence. Our approach offers alternative ways of probing fundamental aspects of classical vectorial light and

improving the efficiency and effectiveness of quantum imaging and communication techniques.

The data that support the findings of this study are available from the corresponding author upon reasonable request.

ACKNOWLEDGMENTS

C.P. and A.F. acknowledge funding from the National Research Fund (NRF), South Africa.

-
- [1] A. Forbes, M. de Oliveira, and M. R. Dennis, *Nat. Photonics* **15**, 253 (2021).
- [2] I. Nape, B. Sephton, P. Ornelas, C. Moodley, and A. Forbes, *APL Photonics* **8**, 051101 (2023).
- [3] S. Franke-Arnold, *Nat. Rev. Phys.* **4**, 361 (2022).
- [4] C. He, Y. Shen, and A. Forbes, *Light Sci. Appl.* **11**, 205 (2022).
- [5] A. Forbes and I. Nape, *AVS Quantum Sci.* **1**, 011701 (2019).
- [6] C. Rosales-Guzmán, B. Ndagano, and A. Forbes, *J. Opt.* **20**, 123001 (2018).
- [7] Y. Shen and C. Rosales-Guzmán, *Laser Photonics Rev.* **16**, 2100533 (2022).
- [8] R. J. C. Spreeuw, *Found. Phys.* **28**, 361 (1998).
- [9] A. Forbes, A. Aiello, and B. Ndagano, *Prog. Opt.* **64**, 99 (2019).
- [10] Q. Zhan, *Adv. Opt. Photonics* **1**, 1 (2009).
- [11] T. Bauer, P. Banzer, E. Karimi, S. Orlov, A. Rubano, L. Marrucci, E. Santamato, R. W. Boyd, and G. Leuchs, *Science* **347**, 964 (2015).
- [12] Y. Shen, E. C. Martínez, and C. Rosales-Guzmán, *ACS Photonics* **9**, 296 (2022).
- [13] I. Nape, K. Singh, A. Klug, W. Buono, C. Rosales-Guzman, A. McWilliam, S. Franke-Arnold, A. Kritzinger, P. Forbes, A. Dudley *et al.*, *Nat. Photonics* **16**, 538 (2022).
- [14] B. Ndagano, B. Perez-Garcia, F. S. Roux, M. McLaren, C. Rosales-Guzman, Y. Zhang, O. Mouane, R. I. Hernandez-Aranda, T. Konrad, and A. Forbes, *Nat. Phys.* **13**, 397 (2017).
- [15] E. Toninelli, B. Ndagano, A. Vallés, B. Sephton, I. Nape, A. Ambrosio, F. Capasso, M. J. Padgett, and A. Forbes, *Adv. Opt. Photonics* **11**, 67 (2019).
- [16] X.-F. Qian and J. Eberly, *Opt. Lett.* **36**, 4110 (2011).
- [17] X.-F. Qian, T. Malhotra, A. N. Vamivakas, and J. H. Eberly, *Phys. Rev. Lett.* **117**, 153901 (2016).
- [18] M. Erhard, M. Krenn, and A. Zeilinger, *Nat. Rev. Phys.* **2**, 365 (2020).
- [19] G. Molina-Terriza, J. P. Torres, and L. Torner, *Nat. Phys.* **3**, 305 (2007).
- [20] A. Mair, A. Vaziri, G. Weihs, and A. Zeilinger, *Nature (London)* **412**, 313 (2001).
- [21] H. Bechmann-Pasquinucci and W. Tittel, *Phys. Rev. A* **61**, 062308 (2000).
- [22] D. S. Tasca, R. M. Gomes, F. Toscano, P. H. Souto Ribeiro, and S. P. Walborn, *Phys. Rev. A* **83**, 052325 (2011).
- [23] A. Acín, N. Brunner, N. Gisin, S. Massar, S. Pironio, and V. Scarani, *Phys. Rev. Lett.* **98**, 230501 (2007).
- [24] C. Reimer, S. Sciara, P. Roztocky, M. Islam, L. Romero Cortés, Y. Zhang, B. Fischer, S. Loranger, R. Kashyap, A. Cino *et al.*, *Nat. Phys.* **15**, 148 (2019).
- [25] S. Ecker, F. Bouchard, L. Bulla, F. Brandt, O. Kohout, F. Steinlechner, R. Fickler, M. Malik, Y. Guryanova, R. Ursin *et al.*, *Phys. Rev. X* **9**, 041042 (2019).
- [26] P.-A. Moreau, E. Toninelli, T. Gregory, and M. J. Padgett, *Nat. Rev. Phys.* **1**, 367 (2019).
- [27] M. P. Almeida, S. P. Walborn, and P. H. Souto Ribeiro, *Phys. Rev. A* **72**, 022313 (2005).
- [28] S. P. Walborn, C. Monken, S. Pádua, and P. S. Ribeiro, *Phys. Rep.* **495**, 87 (2010).
- [29] L. Achatz, E. A. Ortega, K. Dovzhik, R. F. Shiozaki, J. Fuenzalida, S. Wengerowsky, M. Bohmann, and R. Ursin, *Phys. Scr.* **97**, 015101 (2022).
- [30] J. C. Howell, R. S. Bennink, S. J. Bentley, and R. W. Boyd, *Phys. Rev. Lett.* **92**, 210403 (2004).
- [31] M. P. Edgar, D. S. Tasca, F. Izdebski, R. E. Warburton, J. Leach, M. Agnew, G. S. Buller, R. W. Boyd, and M. J. Padgett, *Nat. Commun.* **3**, 984 (2012).
- [32] J. Bavaresco, N. Herrera Valencia, C. Klöckl, M. Pivoluska, P. Erker, N. Friis, M. Malik, and M. Huber, *Nat. Phys.* **14**, 1032 (2018).
- [33] J. Schneeloch, C. C. Tison, M. L. Fanto, P. M. Alsing, and G. A. Howland, *Nat. Commun.* **10**, 2785 (2019).
- [34] H. Defienne, M. Reichert, and J. W. Fleischer, *Phys. Rev. Lett.* **121**, 233601 (2018).
- [35] B. Courme, P. Cameron, D. Faccio, S. Gigan, and H. Defienne, *PRX Quantum* **4**, 010308 (2023).
- [36] N. H. Valencia, V. Srivastav, M. Pivoluska, M. Huber, N. Friis, W. McCutcheon, and M. Malik, *Quantum* **4**, 376 (2020).
- [37] M. McLaren, T. Konrad, and A. Forbes, *Phys. Rev. A* **92**, 023833 (2015).
- [38] A. Selyem, C. Rosales-Guzmán, S. Croke, A. Forbes, and S. Franke-Arnold, *Phys. Rev. A* **100**, 063842 (2019).
- [39] P. Ornelas, I. Nape, R. d. M. Koch, and A. Forbes, [arXiv:2210.04690](https://arxiv.org/abs/2210.04690) [Nature Photonics (to be published)].
- [40] I. Nape, A. G. de Oliveira, D. Slabbert, N. Bornman, J. Francis, P. H. S. Ribeiro, and A. Forbes, *J. Opt.* **24**, 054003 (2022).